J Mater Sci: Mater Electron **(2023) 34:1730**

Flexible piezoresistive sensors and triboelectric nanogenerators based on 3D porous structure PDMS/PPy composites materials

Zhou Qiao[1], Zhiwen Chen[1], Ningqi Luo[1], Aixiang Wei[1,2,*], Yuding He[1], Zhen Liu[1], and Jiaxiong Xu[1]

[1] *School of Integrated Circuits, Guangdong University of Technology, Guangzhou 510006, Guangdong, China*
[2] *School of Information and Intelligent Engineering, Guangzhou Xinhua University, Dongguan 523133, Guangdong, China*

Received: 3 June 2023
Accepted: 10 August 2023
Published online: 29 August 2023

ABSTRACT

Both flexible piezoresistive sensors (FPS) and triboelectric nanogenerators (TENG) have the huge demand for the application in human physiological signals monitoring and human activity monitoring. In this work, the flexible three-dimensional (3D) porous structure polydimethylsiloxane/polypyrrole (PDMS/PPy) composite materials were designed and prepared. The 3D porous structure PDMS/PPy has large surface roughness and sufficient free volume for bulk deformation under pressure loading and unloading. The PDMS/PPy composite materials were used as sensitive materials of FPS and friction layer materials of TENG. The champion FPS based on PDMS/PPy composite materials has a sensitivity of 165.26 kPa^{-1} in the linear region of 200 kPa and long-term stability up to 5500 cycles. The two-electrode contact-separation mode TENG was assembled using Al-PI and PDMS/PPy-ITO. TENG exhibits an output voltage of 6 V, power density of 39.38 $\mu W/cm^2$ and dynamic stability up to 10,000 cycles. This FPS and TENG can be integrated into flexible wearable platforms for self-powered real-time monitoring of physiological signals and human activity.

1 Introduction

With the rapid development of wearable electronic devices, various flexible and stretchable sensors have received significant attention due to their broad promising applications in electronic-skin[1] human–machine interfaces [2], soft robotics [3], artificial intelligence systems [4], human health monitoring [5]. Among these, flexible piezoresistive sensors (FPS) based on various sensitive materials and rational designs have been explored because of their advantages of simplicity in fabrication process and device structure, high sensitivity, high stability, wide linear region, low cost, and easy integration [6, 7]. Although significant researches have been carried out using various nanostructured functional materials (such as nanowires, nanoparticles, nanoribbons, carbon black, carbon nanotubes, and graphene) on different flexible

Zhou Qiao and Zhiwen Chen contributed equally to this study.

Address correspondence to E-mail: weiax@gdut.edu.cn

https://doi.org/10.1007/s10854-023-11131-0

substrates (such as polydimethylsiloxane (PDMS), polyvinylidene fluoride (PVDF), and polyurethane (PU)), it is still a challenge to design and prepare FPS that has both high sensitivity and strong scalability to detect a wide range of human body motions. Because that the physical activity at different positions on the human body will generate different pressure region from a low-pressure region ($P < 10$ kPa) to a medium-pressure region (10 Pa < $P < 100$ kPa) to a high-pressure region ($P > 100$ kPa) [8].

The sensing mechanism of FPS comes from the changes of electrical resistance of the contact interface and the piezoresistive sensing materials itself under an external pressure. The sensitivity S of FPS is defined by the relative resistance changes $\Delta R/R_0$ in response to pressure changes ΔP as $S = \Delta R/R_0 \times 1/\Delta P$ [9]. Conventionally, composite materials based FPS exhibits poor sensitivity and cannot detect in low-pressure range. To improve the sensitivity in a broad pressure range, the FPS based on the micro/nano-structured [10, 11] and porous-structured [12–14] sensing materials have been designed and fabricated. For example, Yin and coworkers [15] fabricated FPS based on the sea urchin-shaped microparticles (SUSM) with a forest of nanostructured spines. The SUSM-based FPS shows ultrahigh sensitive of 121 kPa^{-1} in a linear pressure range of 0–10 kPa and ultralow detection limit of 0.015 Pa and fast response of 7 ms. Ma and coworkers [16] designed a pressure sensor based on a layered structure consisting of PDMS micro-pillars and conductive polyaniline (PANI) nano-pins. Their sensor exhibited an ultra-high sensitivity of 258.7 kPa^{-1} and good environmental stability. Peng and coworkers [17] designed a porous ionogel flexible sensors which exhibited a higher pressure sensitivity, a lower hysteresis (2.4%) and reliable signals during long-term loading (500 cycles). Except for FPS based on micro/nano-structured surfaces and porous-structured materials, other structures and materials based FPS has also been reported. Gong et al. [18] fabricated FPS using sandwiching a gold nanowires (NWs) between two thin PDMS sheets. The gold NWs based FPS shown high sensitivity of 41.14 kPa^{-1}, high stability of 450,000 loading–unloading cycles; low detect pressure of 13 Pa and fast response time of 17 ms.

Most of flexible and stretchable sensors require an external power source. Therefore, the self-powered device is an important requirement for the application of wearable platforms in monitoring of human physiological signals and human activity. The development of flexible and stretchable energy-harvesting devices, which can convert mechanical energy of body movement into electric energy, would be very useful in wearable platforms. Nanogenerators have gained increasing attention because of their ability to harvest electric energy sustainably from environmental energy. Among various types of nanogenerators such as triboelectric, pyroelectric, thermoelectric and piezoelectric nanogenerators, triboelectric nanogenerator (TENG) not only can convert small mechanical energy surrounding environment into electric energy, but also can be easily achieve flexibility [19, 20]. Hence, TENG is very promising self-powered device for useful in wearable platforms. Because of its excellent output performance in harvesting mechanical energy from low frequency motions, TENG has been widely employed as the self-powered device for electronic-skin and wearable platforms. The working mechanism of TENG is based on triboelectrication and electrostatic induction to transform environmental energy (for instance, water wave energy [21, 22], wind energy [23], mechanical energy generated through body movement and some other mechanical movements [24]) into electric energy [25]. Usually, the core structure of TENG is composed of two friction layers with opposite polarity and two electrode layers. The friction layers are used to generate polarized charges during the contact movement. The two electrode layers are used to balance the potential difference in the electrostatic induction process and external current. When the two friction layers come into mechanical contact, triboelectric charges are generated and uniformly distributed on their surfaces. While the friction layers are separated, the induction charges will be generated on the electrode layers. The electrostatic potential difference established by the triboelectric charges on the triboelectric layers will drive the current to flow through external circuit. In general, the triboelectric layer materials employed in TENG are chosen based on their triboelectric polarity for achieving high electric output. A wide variety of materials have been used as friction layers for TENG, such as PDMS, nylon, cotton, paper (plant fiber), and aluminum are often used as friction layers with positive polarity, while polyvinylidene fluoride (PVDF), polyimide (PI), and polyethylene terephthalate (PET) are widely used as friction layers with negative polarity [26, 27].

The electrical performance of TENG is usually characterized by open circuit voltage, short circuit current and power density. Compared to other types

of nanogenerators, the power density of TENG is relatively small because of the small current generated by TENG. According to the working mechanism of TENG, the amount of induced charges is related with the amount of triboelectrification charges. The surface structure and composition of friction layer materials play key roles in increasing the amount of triboelectrification charges. Therefore, there are three material strategies to enhance the performance of TENG. The first strategy of improving the electrical performance of TENG is to enlarge the surface area of the friction layer by fabricating the surface microstructures, such as nanoparticles or nanowires [28, 29]. The second strategy of improving the electrical performance of TENG is to develop porous structures inside the friction layers using pore foaming technology, such as particle templates methods [30, 31]. This approach was cheap and simple. For example, Lee et al. [30] reported the sponge structure PDMS film based TENG with a very large output voltage of 130 V and current density of 0.10 mA cm^{-2}. The third strategy of improving the electrical performance of TENG is to modify the surface of friction layers with some fluorochemical or nitrogenous compounds to change its polarity [32, 33]. For example, Wang et al. [34] reported that the output power of TENG is enhanced by approximately 4 times by using self-assembled thiol molecules with amine as the head group to functionalize Au surfaces. In addition, Feng and coworkers [27] developed a newly structured TENG consisting of friction layer, electrode layer, and a charge storage intermediate layer. The output performance of their TENG was improved by an order of magnitude due to adding a polyimide (PI) as a charge storage intermediate layer between the friction layer and the electrode layer.

In this work, we developed a material strategy to prepare the three-dimensional (3D) porous structure PDMS/PPy composite materials. First, 3D PPy network was grown on commercial Ni foam by electrodeposition method, where the thickness of PPy can be tuned by varying the electrodeposition time. Second, a PDMS matrix was infiltrated into the pores of PPy-Ni foam. Finally, after the PDMS curing process, the PDMS-PPy-Ni foam was immersed into a mixed solution of HCl and FeCl to etch away Ni and obtain the final porous structure PDMS/PPy composite films. The fabrication processes of the 3D porous structure PDMS/PPy possess three distinctive characteristics. (1) The support of the rigid Ni scaffold preserve the surface roughness of the composite film after the PDMS infiltration process, leading to big change of contact resistance between the composite film and metal electrodes caused by the external pressure loading. (2) It leaves sufficient free volume for bulk deformation under pressure loading and unloading. (3) The electrical conductivity and mechanical elasticity of the PDMS/PPy composite films can be tuned separately by varying the thickness of PPy and the PDMS prepolymer to cross-linker ratio, respectively. As a result, FPS based on PDMS/PPy composite materials has a sensitivity of 165.26 kPa^{-1} in a 100 kPa linear region. In addition, we find that the 3D porous structure PDMS/PPy composite materials have also the triboelectric effect. The dual-electrode contact-separation mode TENG was assembled using Al-PI and PDMS/PPy-ITO. The electrical performance and stability of TENG were measured and discussed. The porous structure of PDMS/PPy composite materials can improve the sensitivity and working range of FPS as well as the amount of triboelectrification charges of TENG.

2 Experimental sections

2.1 Preparation of 3D porous structure PDMS/PPy composite materials

Fabrication flow of 3D porous structure PDMS/PPy composite materials is illustrated in Fig. 1a. PDMS/PPy composite materials with 3D porous structures were prepared in three steps. The first step, the polypyrrole (PPy) was deposited on commercial Ni foam (thickness of 1.5 mm) by electro-deposition method using Ni foam as working electrode and platinum sheet as counter electrode. The Ni foam was cleaned by ultrasonic sequentially in acetone and deionized water for 30 min each and was dried at 80 °C for a few min before electrodeposition. The electrolyte solution was prepared by dissolving 5 mmol sodium p-toluenesulfonate, 5 mmol sodium perchlorate, and 800 µl pyrrole monomer into 100 ml deionized water. The thickness of PPy was controlled by varying the electro-deposition time from 15, 20, 30, 40 to 50 min. The second step, the PDMS solution was prepared by mixing prepolymer with cross-linker (mass ratio of 10:1) and subsequently magnetically stirring for 2 h, and then the PDMS solution was infiltrated into the pores of PPy-Ni foam. To let PDMS solution fully infiltrate PPy-Ni foam, the PDMS-PPy-Ni foam was pumped under vacuum for 2 h. After infiltration, the filled PDMS-PPy-Ni foam was cured at 90 °C for 1 h,

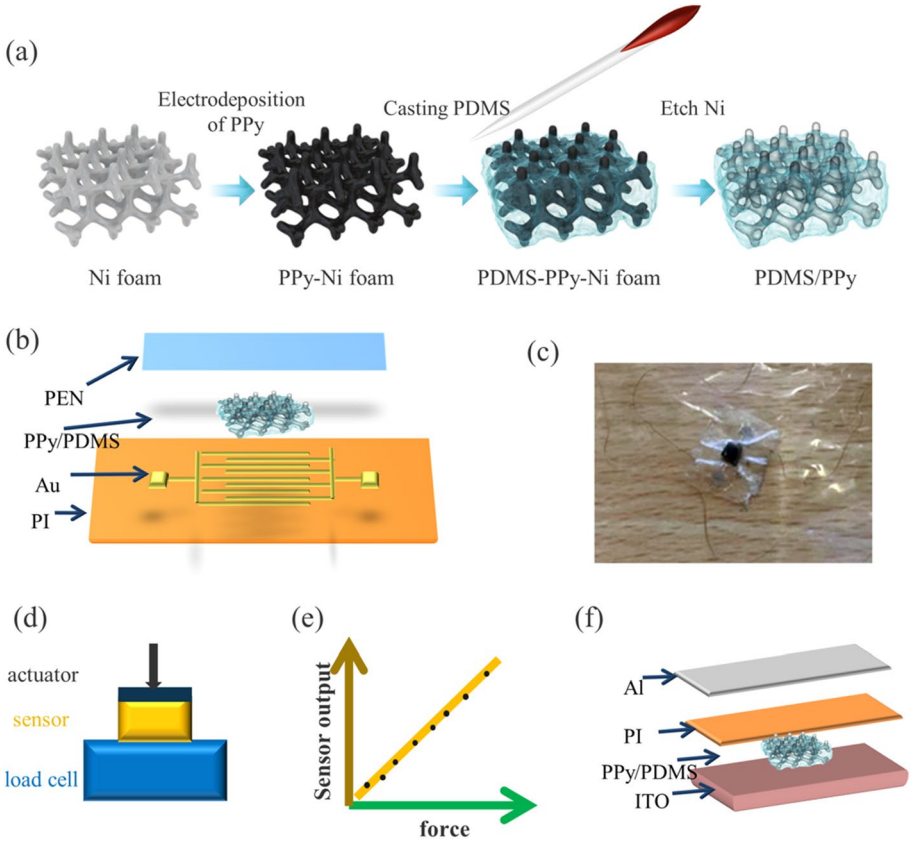

Fig. 1 **a** Fabrication process of 3D porous structure PDMS/PPy composite materials; **b** material and sandwich structure of the FPS, **c** photograph of the as-assembled FPS; **d** illustration of the calibration process for FPS; **e** pressure response curves of sensor; **f** material and structure of the TENGs

and then cooled to room temperature. The third step, to etch away Ni skeleton from the PDMS-PPy-Ni foam, the etching solution containing 30 wt.% $FeCl_3$ and 1 M HCl was prepared. The PDMS-PPy-Ni foam was soaked in etching solution for 48 h. Finally, the PDMS/PPy composite materials were cleaned in deionized water, and dried at 80 °C for a few min. The obtained 3D porous structure PDMS/PPy composite materials were used as the piezoresistive sensing materials of FPS and the friction layer materials of TENG.

The scanning electron microscopy (SEM, SU8010, Hitachi) was used observed the morphology of 3D porous structure PDMS/PPy composite materials. Energy dispersive spectrometry (EDS, SU8010, Hitachi) was used to analyze element distribution map of PDMS/PPy composite materials. Infrared spectrometry (Nicolet 6700) was used to analyze the structure of PDMS/PPy composite materials.

2.2 Fabrication and calibration of FPSs based on 3D porous structure PDMS/PPy composite materials

The FPS with horizontal electrode structure (Fig. 1b) was assembled using the PDMS/PPy composite materials, Au fork-finger electrode patterned on a polyimide (PI) substrate, and encapsulated by a 1.4 μm polyethylene (PEN) film. The optical photograph of the as-prepared FPS was provided in Fig. 1c. The basic parameters of the Au fork-finger electrodes are electrode width of 200 μm, interval of 10, 20, 50, and 100 μm, respectively, active pressure sensitive area of 10 mm × 10 mm. The calibration method of FPS has been introduced in our previous work [6]**.** During the calibration, the sensor was placed between the piezoelectric actuator and load cell as shown in Fig. 1d. The pressure applied to the sensor is generated by the movement of the piezoelectric actuator. Meanwhile the value of pressure was measured by the load cell. A steady voltage of 1 V was used to drive FPS, and the

output current of FPS was tested using the Keithley 2636B source meter. The applied pressure and current were simultaneously recorded using a LabVIEW program as shown in Fig. 1e.

2.3 Fabrication and measurement of TENG based on the PDMS/PPy composite materials

The dual-electrode contact-separation mode TENG was assembled using PI and PDMS/PPy as fraction layers, Al and ITO as conductive layers. The PDMS/PPy composite materials were attached onto the ITO glass as friction electrode; a thin PI film was firmly adhered to Al foil tape as the other friction pair electrode to form Al-PI@PDMS/PPy-ITO TENG. Schematic of the dual-electrode contact–separation Al-PI@PDMS/PPy-ITO TENG was shown in Fig. 1d. The contact and separation of Al-PI and PDMS/PPy-ITO of TENG were controlled by a magnetostrictive rod. The triboelectric potential difference generated between the two electrode layers during the contact and separation process will drive the current to flow through external circuit. The output voltage was measured by a Tektronix oscilloscope (model TBS2000B).

3 Results and discussion

3.1 Characterization of 3D porous structure PDMS/PPy composite materials

The morphology of samples was observed using field emission scanning electron microscopy. Figure 2 shows the SEM images of Ni foam, PPy-Ni foam, PDMS-PPy-Ni foam, and 3D porous structure PDMS/PPy composite materials, respectively. Compared Fig. 2b with Fig. 2a, it can be observed that the thin PPy is deposited on Ni foam. In addition, after electrodepositing PPy, the color change from grayish Ni foam to brown PPy-Ni foam can also be used to determine that PPy has been deposited on Ni foam. The pores inside the PPy-Ni foam are fully filled with PDMS as indicated in Fig. 2c. The SEM image of the PDMS/PPy composite materials shown in Fig. 2d indicates that the composite materials maintain a rough surface. PDMS serves as mechanical support for the porous structure PDMS/PPy composite materials; therefore, PDMS should be fully filled into the pores inside the PPy-Ni foam during the PDMS infiltration process. In the meantime, the surface roughness of the foam should be remained to achieve high sensor response of FPS.

To prove that the foam Ni skeleton has been etched away, the energy dispersive spectroscopy (EDS) was

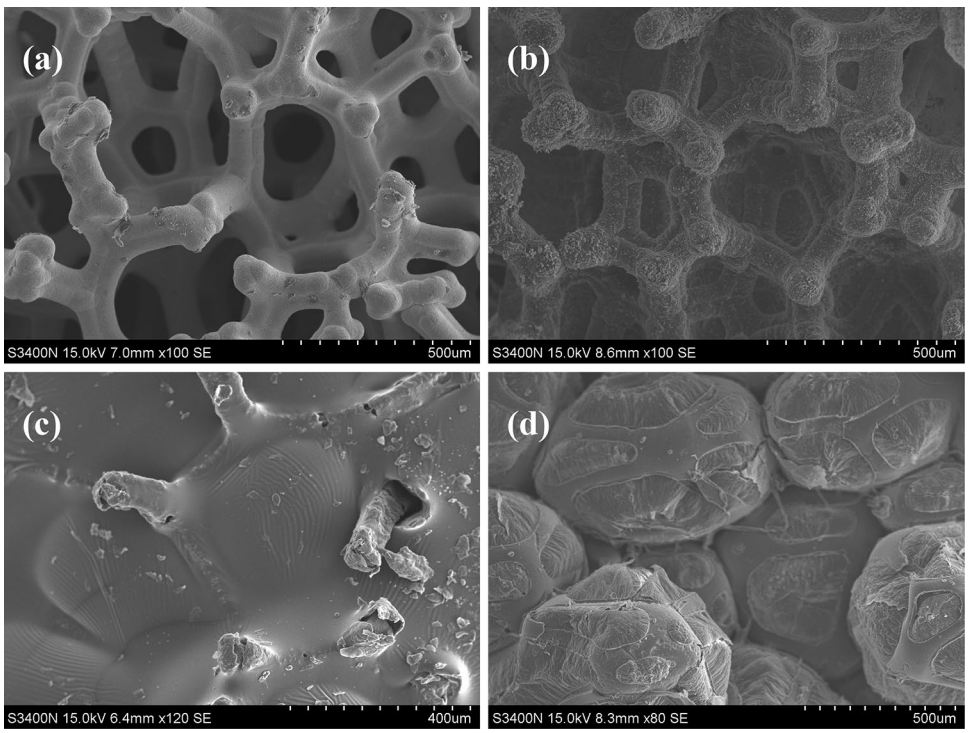

Fig. 2 SEM image of **a** Ni foam; **b** PPy-Ni foam; **c** PDMS-PPy-Ni foam (with Ni skeleton); **d** PDMS/PPy composites materials (etching away Ni skeleton)

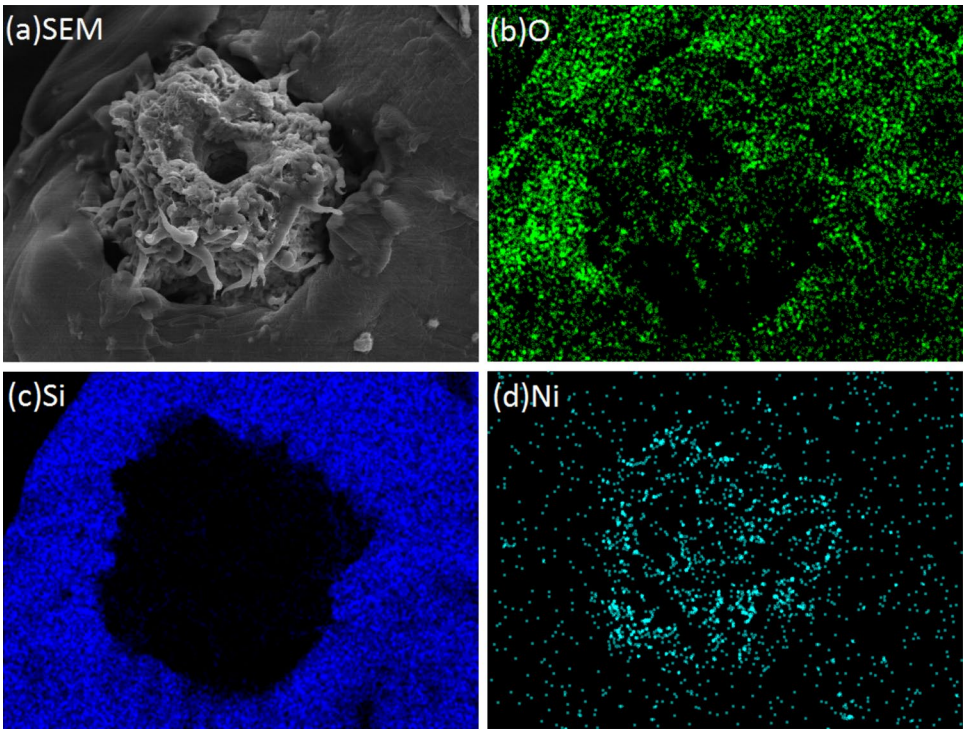

Fig. 3 **a** Low-magnification SEM image; **b–d** EDS element mapping images of PDMS/PPy composite materials

used to analyze the chemical composition and elemental mapping images of the PDMS/PPy composite materials. We know that PDMS is made of elements C, H, O, Si, and PPy is made of elements C and N. The result of EDS elementals analysis indicated that the atomic percentage of elements C, O, Si, Ni, Fe, and Cl is 48.46, 25.88, 20.30, 0.55, 1.10, and 3.71%, respectively. The Ni atomic percentage of 0.55% suggests that the Ni foam skeleton has been etched away. A few Fe and Cl come from the residual etch solution. Figure 3 displays SEM images and the corresponding O, Si, and Ni elemental mappings of PDMS/PPy composite materials. As can be observed in Fig. 3, the dense Si and O elements from PDMS are uniformly distributed around the pore, while Ni and O elements are sparsely distributed on position of the pore, indication that the Ni foam skeleton has been etched away. O elements distributed on position of the pore should come from air. To further confirm that PPy was introduced into the composite materials, the Fourier-transform infrared (FTIR) spectra of PPy, PDMS, and PDMS/ PPy composite materials are shown in Fig. 4. The FTIR characteristic peak of PPy is located at 1631 cm^{-1}, while the FTIR characteristic peaks of PDMS are located at 757, 795, 844, 865, 1016, 1072, and 1259 cm^{-1}, respectively. Compared the FTIR characteristic peaks of PPy, PDMS and PDMS/PPy shown in Fig. 4, it can be observed that the PDMS/PPy has FTIR characteristic peaks of both PPy and PDMS, indicating further that the PDMS/PPy composite materials can be successfully prepared by the fabrication process depicted in Fig. 1a.

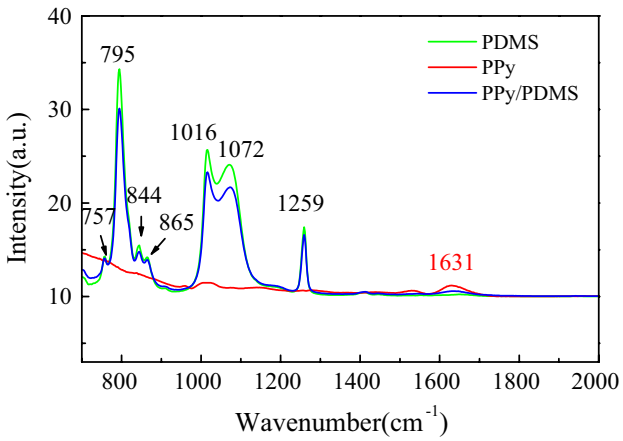

Fig. 4 FTIR spectra of PPy, PDMS and PPy/PDMS composite materials

3.2 FPS based on 3D porous structure PDMS/PPy composite materials

3.2.1 Sensing mechanism of FPS based on 3D porous structure PDMS/PPy composite materials

Sensing mechanism of FPS with the horizontal electrode structure is displayed in Fig. 5a. Under applied pressure loading, the contact points among the PPy conductive networks inside PDMS/PPy as well as the contact points between the rough surface of PDMS/PPy and the gold electrode increase as shown in Fig. 5a, therefore, the bulk resistance R_b of PPy/PDMS itself and contact resistance R_c between the PDMS/PPy composite materials and Au electrode decrease, resulting in an increase output current when FPS is driven by a steady voltage. In contrast, under applied pressure unloading, both the bulk resistance R_b and contact resistance R_c increases, resulting in a reduce output current.

The sensitivity and linearity region of FPS are important indicators. The sensitivity S of FPS is defined as the resistance changes $\Delta R/R_0$ in response to pressure changes ΔP, or the output current changes $\Delta I/I_0$ in response to pressure changes ΔP because device is driven by a constant voltage [9, 35].

$$S = \frac{\Delta R}{R_0 \Delta P} = \frac{\Delta I}{I_0 \Delta P} \quad (1)$$

where S represents the sensitivity in kPa^{-1}; P is applied pressure; I_0 and R_0 are the initial current and resistance of FPS working without applied pressure. ΔI and ΔR are the changes in current and resistance of FPS under applied pressure loading. Therefore, the sensitivity of FPS can be obtained according to the slope of the pressure response curve. The large resistance variation upon pressure changes result in good sensor response.

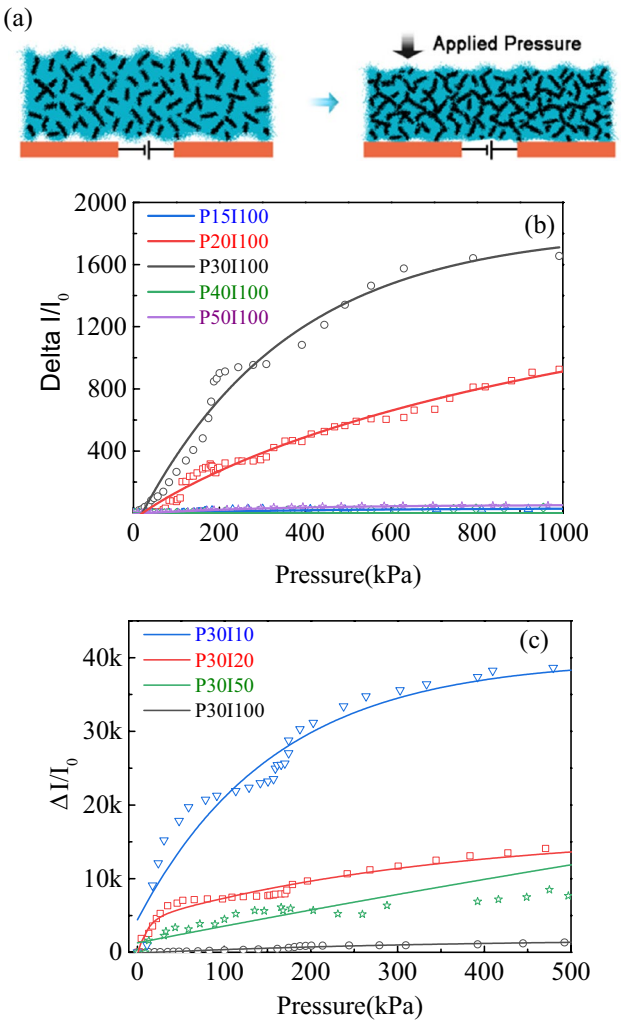

Fig. 5 **a** Schematic illustration of sensing mechanisms of piezoresistive sensor with horizontal electrode design; **b** pressure response curves of FPS based on PDMS/PPy composite material. PDMS/PPy was prepared at different growth times of 15 20, 30, 40 and 50 min, while keeping a fixed electrode interval of 100 μm; **c** pressure response curves of FPS. FPS was fabricated using different electrode interval of 10, 20, 50 and 100 μm while keeping a fixed PDMS/PPy growth times of 30 min

3.2.2 Sensor performance of FPS based on 3D porous structure PDMS/PPy composite materials

To investigate the effect of growth time of PPy and interval of fork-finger electrodes on performance of FPS, two sets of FPS based on PDMS/PPy composite materials were fabricated. The first set of FPS were fabricated using the PDMS/PPy with different PPy growth times of 15, 20, 30, 40, and 50 min while keeping a fixed electrode interval of 100 μm (labeled as P15I100 to P50I100). The second set of FPS were fabricated using different electrode interval of 10, 20, 50, and 100 μm while keeping a fixed PPy growth time of 30 min (labeled as P30I10 to P30I100). The pressure response curves of two sets of FPS are shown in Fig. 5b and c, respectively. In Fig. 5b, the PPy with different thickness was prepared at various deposition time of PPy. The deposition time of PPy has a significant effect on the sensitivity of FPS. The deposition time of PPy increase from 15 min, 20 min to 30 min, the sensitivity

of FPS gradually increase. When deposition time of PPy is 30 min, the sensitivity reaches the maximum value of 4.74 kPa^{-1} in a 200 kPa linear range. Afterward, the sensitivity of FPS gradually decreased when deposition times of PPy further extended to 40 min and 50 min, which is because that the sensitivity of FPS is determined by the change rate of the resistance upon pressure changing. Firstly, the conductive network of PPy inside the porous structure PDMS/PPy composites materials can be regulated by varying the PPy deposition time. The electrical conductivity of PDMS/PPy composites materials increased with prolonging deposition time of PPy. The sensitivity of FPS is determined by the change rate of the resistance. Therefore, the biggest resistance variation upon applied pressure changes results in the maximum sensitivity of FPS. Figure 5c provides the pressure response curves of FPS fabricated using different electrode interval of 10, 20, 50, and 100 μm while keeping a fixed PDMS/PPy growth time of 30 min. When the electrode interval decrease from 100 μm to 10 μm, the sensitivity of the devices increases drastically from 4.74 kPa^{-1} to 165.26 kPa^{-1}. However, the linear region of FPS basically keeps the same (200 kPa). The effect of the electrode interval on the sensitivity of FPS mainly comes from the changes of contact resistance between PDMS/PPy and the gold electrode. The active pressure sensitive area (10 mm × 10 mm) and the electrode width are fixed, the smaller electrode interval is, the larger the total contact area between PDMS/PPy and gold electrode. Under applied pressure loading, the number of contact points has large changes, resulting in a large resistance changes (as shown in Fig. 5a) and a high sensitivity of FPS. In addition, because the PDMS/PPy composites materials were prepared at the fixed ratio (10:1) of PDMS prepolymer to cross-linker, the mechanical properties (such as elasticity and Young's modulus) of PDMS/PPy remain basically the same, resulting in the line range of FPS basically unchanging. The effect of the PDMS prepolymer to cross-linker ratio on mechanical properties of PDMS/PPy and linear region of FPS will further be studied in the future.

According to the results of Fig. 5b and c, the conclusion can be proved that FPS (P30I10) prepared at the PPy deposition time of 30 min and the electrode interval of 10 μm has the highest sensitivity of 165.26 kPa^{-1} in a wide linear range of 200 kPa. The preparation sequence shown in Fig. 1a is very important for improving sensing performance of FPS. The PDMS was infiltrated prior to Ni scaffold etched away which maintain rough surface of the PDMS/PPy composite materials and form 3D porous structure, leaves sufficient free volume for bulk deformation. In addition, the smaller electrode interval can provide more contact points between PDMS/PPy and electrode under same active pressure sensitive area.

The response speed, stability, and durability of FPS are also critical for practical applications. To investigate the response speed of device, response curve of the champion FPS (P30I10) under loading and unloading over a period is displayed in Fig. 6a, and the response time of FPS is 385 ms for loading and 62 ms for unloading. Meanwhile, Response curves of the champion FPS (P30I10) when it is periodically "pressed" and "released" under different frequencies and different pressures are shown in Fig. 6b and c, respectively. The device has an identifiable response curve at different frequencies (Fig. 6b) and different pressures (Fig. 6c). The stability measurement of the champion FPS (P30I10) was carried out at a fixed trigger frequency of 1 Hz and a fixed applied pressure of 1 N, the result is displayed in Fig. 6d. FPS shows long-term stability up to 5500 cycles, indicating superior durability and repeatability of FPS.

3.2.3 *Application of FPS based on 3D porous structure PDMS/PPy composite materials*

To investigate the application of the PDMS/PPy sensor, four examples of practical applications are provided. FPS is driven by steady voltage of 1 V in the following four practical applications. In the first application, FPS is attached to the wrist of a human body to record the physiological signals. The wrist signals measured by FPS (Fig. 7a) have similar features with the actual arterial blood pressure pulses. Therefore, FPS based on PDMS/PPy can be employed as a measurement unit in a blood pressure measurement device and has future potential as a real-time dynamic wearable blood pressure monitor. In the second application, the PDMS/PPy sensor is attached to the finger joint, when the finger joint bent at different angles (45° and 90°) the sensor has a different response, Fig. 7b displays the pulse signals recorded by FPS. In the third application, the PDMS/PPy sensor is attached to the fingertip to record the pulse signals produced by the fingertip clicking any object. Figure 7c shows the pulse signals recorded by FPS when the fingertip click desk.

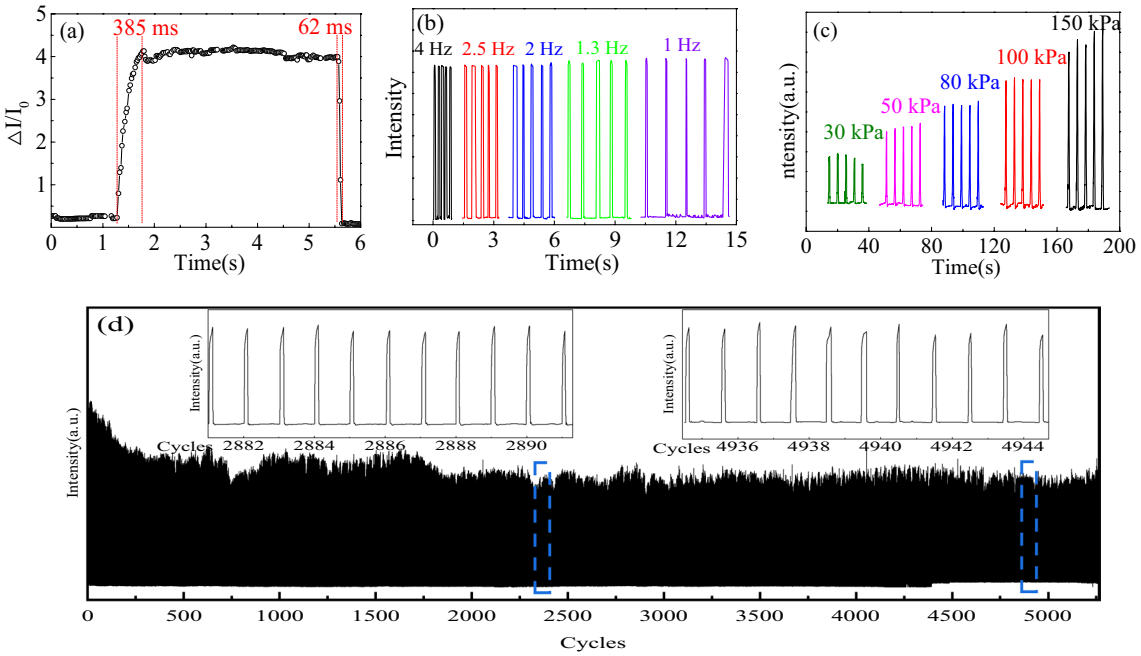

Fig. 6 **a** Response time of the champion sensor under loading and unloading over a period; **b** response curves of the champion FPS when it is periodically pressed and released under different frequency; **c** response curves of the champion FPS under different pressures; **d** 5500 cycles stability of the champion sensor under 1 Hz trigger

Fig. 7 Applications of FPSs. **a** Wrist pulse signals recorded by a sensor; **b** pulse signals recorded by sensor attached to the finger joint when the finger joint bend at 45° and 90°; **c** pulse signals recorded by sensor attached to the fingertip when the fingertip click desk; **d** pulse signals recorded by sensor under various bending status

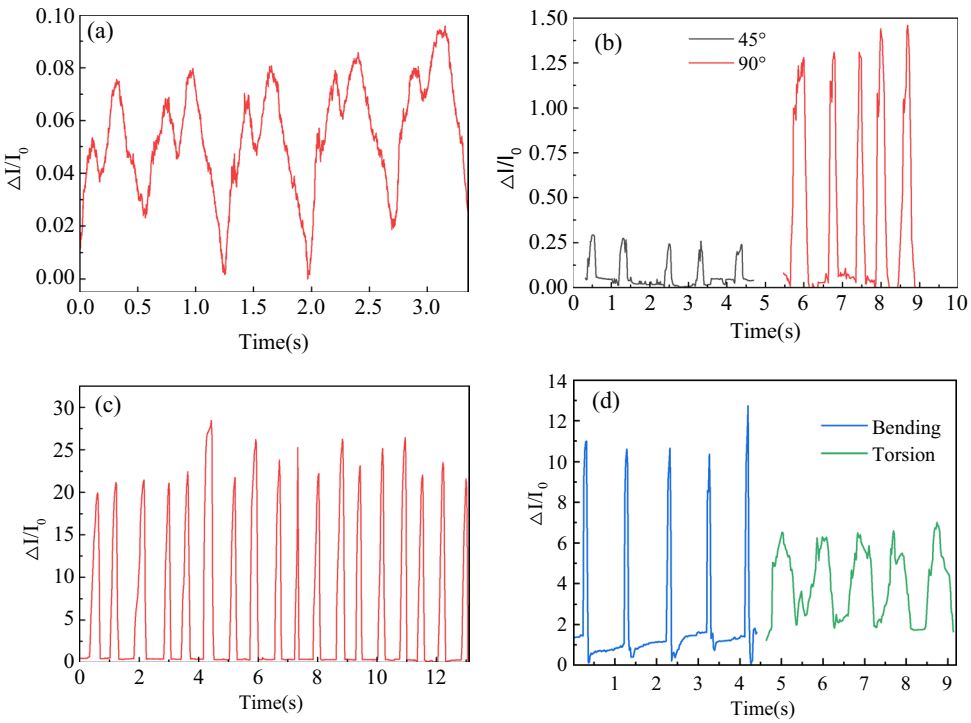

In Fig. 7b and c, the PDMS/PPy sensor shows a timely, sensitive, and stable force feedback. Therefore, it has future potential as a force feedback sensing unit for machine hand operation. In the fourth application, the PDMS/PPy sensor response is calibrated under various bending status, the response curve are shown in Fig. 7d. Therefore, the PDMS/PPy sensor can be can be used for e-pulse monitoring and the e-skin application due to its mechanical flexibility.

3.3 Operating mechanism and output performance of TENG based on 3D porous structure PDMS/PPy composite materials

TENG contains two parts, the top layer of Al-PI friction electrode as negative part and the bottom layer of PDMS/PPy-ITO as positive part. The structure of Al-PI@PDMS/PPy-ITO TENG and its operating principle are shown in Fig. 8. In the initial state, there is no any electric charge in the PDMS/PPy and PI friction layers due to no contact between PDMS/PPy and PI, as shown in Fig. 8a. When PDMS/PPy friction layer is in full contact with PI friction layer, triboelectric charges are generated because they have different electron affinities. The positive charges are uniformly distributed on PDMS/PPy surface and equal negative charges are uniformly distributed on PI surface, as shown in Fig. 8b. In this state, all charges are in the same plane; thus, the TENG is in an electrical neutral state. When the PDMS/PPy friction layer is separated from PI friction layer, TENG is no longer in electrical equilibrium.

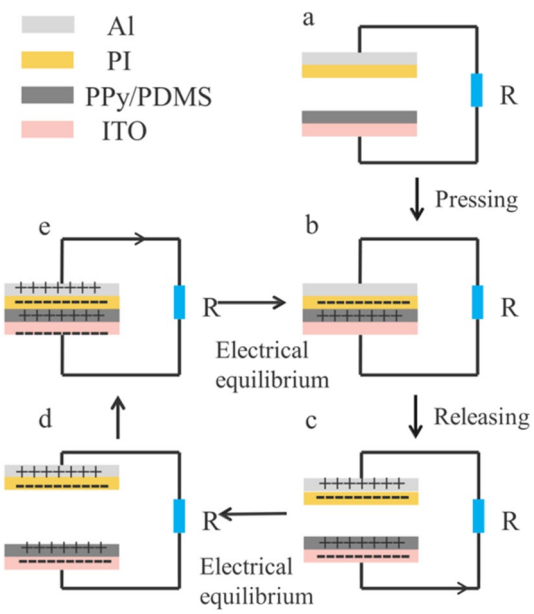

Fig. 8 Illustration of the working mechanism of contact-separation mode Al-PI@PDMS/PPy-ITO TENG: **a** initial; **b** contact; **c** releasing; **d** fully released; **e** pressing states

Due to the electrostatic induction effect, the electrons move from the Al electrode through R to ITO electrode driven by the electric potential difference until TENG reaches electrical equilibrium, as shown in Fig. 8c and d. Once TENG reaches electrical equilibrium, the current through the external circuit is 0. When the TENG is pressed again, the electrons move from the ITO electrode through R to Al electrode, as shown in Fig. 8e. Therefore, because of the coupling of triboelectrification and electrostatic induction, AC electrical output is generated during a contact-separate process of TENG. The electrical properties of TENG (such as open circuit voltage, short circuit current, and power density) depend on the density of charges generated by the friction electrodes.

The Al-PI@PDMS/PPy-ITO TENG was fabricated as described in previous Sect. 2.3. The effective area of TENG is 25 mm^2. To evaluate the frictional electrical properties of TENG, the output performance of Al-PI@PDMS/PPy-ITO TENG was measured in contact and separation model. The contact and separation of the Al-PI electrode and PDMS/PPy-ITO electrode were driven by a magnetostrictive rod under different frequencies. Figure 9a provides output voltage V_{OC} of TENG measured under different frequencies. During periodical contact and separation, TENG generates symmetric output voltage of approximately 6 V. The frequency has no effect on the value of output voltage of TENG. However, higher frequencies can reduce the errors, so subsequent measurements are performed under a frequency of 4 Hz. To study the output performance under different external loads R, the output voltage and output current were tested under various values of the loading resistances R when periodically contact and separation under a frequency of 4 Hz. The output power density (P) is calculated through the equation

$$P = \frac{IV}{A} \tag{2}$$

where P represents power density; I and V are the output current and voltage, A is the effective area of TENG. Figure 9b shows the resistance dependences of both the output voltage and power density of TENG with the loading resistances from 1 MΩ to 100 MΩ.

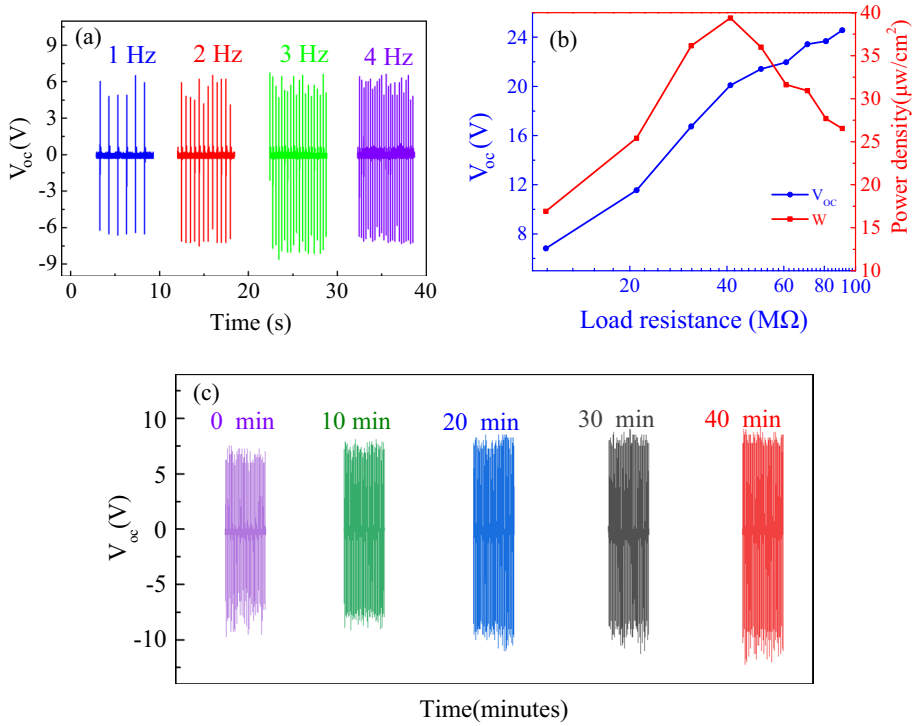

Fig. 9 **a** The output voltage performance of Al-PI@PDMS/PPy-ITO TENGs drived under different contact frequency; **b** the output voltage and power density of Al-PI@PDMS/PPy-ITO TENGs under different load resistance; **c** stability of TENGs for over 10,000 contact-separations cycles

As shown in the Fig. 9b, the output voltage linearly increases as R increases from 1 MΩ to 100 MΩ, whiles its power density first increases and then decreases as the load resistance increases. The maximum power density of Al-PI@PDMS/PPy-ITO TENGs is 39.38 μW/cm^2 under the loading resistances of 41 MΩ. TENG is a power supply. According to Ohm's law, the current, output voltage, and power are given by

$$I = \frac{\varepsilon}{R + r} \tag{3}$$

$$V = \varepsilon - Ir \tag{4}$$

$$P = IV = \frac{\varepsilon}{R + r} \times \left(\varepsilon - \frac{\varepsilon r}{R + r}\right) \tag{5}$$

$$\text{Let } \frac{\partial P}{\partial R} = 0, \text{ give } R = r \tag{6}$$

where I, V, and P are the output current, voltage, and power, respectively. ε and r are electromotive force and internal resistance of TENG. R is the loading resistance. According to Eqs. (3) and (4), the output voltage V_{oc} increases as loading resistance R increases. According to Eqs. (5) and (6), the power density P reaches its maximum value when $R = r$.

As a triboelectric nanogenerator, stable and continuous power output is an important factor for practical applications, so the stability of Al-PI@PDMS/PPy-ITO TENG was tested for 10,000 cycles at an operating frequency of 4 Hz and a fixed load resistance of 41 MΩ. The duration of the test was 40 min intercepting the open-circuit voltage output signals at 0 min, 10 min, 20 min, 30 min, and 40 min, respectively. As shown in Fig. 9c, the TENG exhibits excellent stability. It was continuously contact and separation for 40 min at 4 Hz, The output voltage V_{oc} remains stable at approximately 8 V during the entire cycles.

4 Conclusion

In summary, 3D porous structure PDMS/PPy composite materials were designed and fabricated. The material preparation process designed in this work not only keeps the surface roughness of PDMS/PPy composite materials, but also leaves sufficient free space for the body deformation under applied pressure. 3D porous structure PDMS/PPy composite materials were used as sensitive material of FPS and friction layer material of TENG. Their porosity is very important to improve the performance of both FPS and TENG. The champion FPS based on PDMS/PPy composite materials

has a sensitivity of 165.26 kPa^{-1} in the linear region of 200 kPa and long-term stability up to 5500 cycles. The sensor has a loading response time of 385 ms and an unloading response time of 62 ms. The Al-PI@PDMS/PPy-ITO two-electrode contact-separation mode TENG exhibits an output voltage of 6 V, power density of 39.38 $\mu W/cm^2$, and dynamic stability of over 10,000 cycles. The design and fabrication strategy of the bifunctional flexible material have great potential for the practical applications in flexible wearable platforms for self-powered real-time monitoring of physiological signals and human activity.

Author contributions

Material preparation, data collection and analysis were performed by Zhou Qiao, Zhiwen Chen, Ningqi Luo and Aixiang Wei. The first draft of the manuscript was written by Zhou Qiao, Zhiwen Chen. All authors contributed to the study conception and design. All authors commented on previous versions of the manuscript. All authors read and approved the final manuscript.

Funding

This work has been financially supported by the National Science Foundation of China (No. 61904040).

Data availability

The data that support the findings of this study are available on request from the corresponding author.

Declarations

Conflict of interest There are no conflicts to declare.

Financial interests All authors have no relevant financial or non-financial interests to disclose.

Compliance with ethical standard The paper reflects the authors' research and analysis in a truthful and complete manner.

Informed consent Not applicable in this research.

References

1. C. Hou, Y. Liu, R.S. Liu, X.C. Liang, Z.T. Wu, Z.H. Wu, Nano Energy **97**, 107189 (2022)
2. Q. Shu, S. Liu, J.P. Wu, H.X. Deng, X.L. Gong, S.H. Xuan, Chem. Eng. J. **433**, 134424 (2022)
3. Y.F. Meng, Y.J. Ma, X. Feng, A.C.S. Appl, Electron. Mater. **2**, 3577 (2020)
4. Y. Chen, G. Gao, J. Zhao, H. Zhang, J. Yu, X. Yang, Q. Zhang, W. Zhang, S. Xu, J. Sun, Y. Meng, Q. Sun, Adv. Funct. Mater. **29**, 1 (2019)
5. Y. Khan, A.E. Ostfeld, C.M. Lochner, A. Pierre, A.C. Arias, Adv. Mater. **28**(22), 4373 (2016)
6. Z. Qiao, A.X. Wei, K.D. Wang, N.Q. Luo, Z. Liu, J. Alloys Compd. **917**, 165503 (2022)
7. Q.B. Zheng, J.H. Lee, X. Shen, X.D. Chen, J.K. Kim, Mater. Today **36**, 158 (2020)
8. T.Q. Trung, N.E. Lee, Adv. Mater. **28**, 4338 (2016)
9. T. Dinh, T. Nguyen, H.P. Phan, N.T. Nguyen, D. Viet Dao, J. Bell, Biosens. Bioelectron. **166**, 112460 (2020)
10. M.M. Liu, X. Pu, C. Jiang, T. Liu, X. Huang, L. Chen, C. Du, J. Sun, W. Hu, Z.L. Wang, Adv. Mater. **29**, 17037009 (2017)
11. J.F. Shu, R.R. Yang, Y.Q. Chang, X.Q. Guo, X. Yang, J. Alloys Compd. **879**, 160466 (2021)
12. X.P. Li, Y. Li, X. Li, D. Song, P. Min, C. Hu, H.-B. Zhang, N. Koratkar, Z.-Z. Yu, J. Colloid Interface Sci. **542**, 54 (2019)
13. J. Li, S. Orrego, J. Pan, P. He, S.H. Kang, Nanoscale **11**, 2779 (2019)
14. A. Tewari, S. Gandla, S. Bohm, C.R. McNeill, D. Gupta, ACS Appl. Mater. Interfaces **10**, 51859 (2018)
15. B. Yin, X. Liu, H. Gao, T. Fu, J. Yao, Nat. Commun. **9**, 5161 (2018)
16. L.S. Yan Ma, M. Chen, Z. Li, L.M. Wu, Chem. Eng. J. **441**, 136028 (2022)
17. S.Q. Peng, Q.Q. Guo, N. Thirunavukkarasu, Y.L. Zheng, Z. Wang, L.H. Zheng, L.X. Wu, Z.X. Weng, Chem. Eng. J. **439**, 135593 (2022)
18. S. Gong, W. Schwalb, Y. Wang, Y. Chen, Y. Tang, J. Si, B. Shirinzadeh, W. Cheng, Nat. Commun. **5**, 3132 (2014)
19. X. Chen, L. Luo, Z. Zeng, J. Jiao, M. Shehzad, G. Yuan, H. Luo, Y.J. Wang, Materiomics **6**, 643 (2020)
20. J.B. Yu, L. Chen, X.J. Hou, J.L. Mu, J. He, W.P. Geng, X.J. Qiao, X.J. Chou, J. Materiomics **8**, 247 (2022)
21. Z.H. Lin, G. Cheng, S. Lee, K.C. Pradel, Z.L. Wang, Adv. Mater. **26**, 4690 (2014)
22. X. Zhang, Y. Zheng, D. Wang, Z.U. Rahman, F. Zhou, Nano Energy **30**, 321 (2016)

23. L. Zhang, B. Zhang, J. Chen, L. Jin, W. Deng, J. Tang, H. Zhang, H. Pan, M. Zhu, W. Yang, Z.L. Wang, Adv. Mater. **28**, 1650 (2016)
24. M. Zhang, T. Gao, J.S. Wang, J.J. Liao, Y.Q. Qiu, Q. Yang, H. Xue, Z. Shi, Y. Zhao, Z.X. Xiong, L.F. Chen, Nano Energy **13**, 298 (2015)
25. M. Kim, C.J. Lee, S.H. Kim, M.U. Park, J. Yang, Y. Yi, K.H. Yoo, J. Mater. Chem. A **9**, 10316 (2021)
26. Y.J. Kim, X.W. Wu, J.H. Oh, Sci. Rep. **10**, 2742 (2020)
27. Y.G. Feng, Y.B. Zheng, G. Zhang, D.A. Wang, F. Zhou, W.M. Liu, Nano Energy **38**, 467 (2017)
28. S. Jang, H. Kim, J.H. Oh, Nanoscale **9**, 13034 (2017)
29. G. Zhu, Z.H. Lin, Q.S. Jing, P. Bai, C.F. Pan, Y. Yang, Y.S. Zhou, Z.L. Wang, Nano Letter **13**, 847 (2013)
30. K.Y. Lee, J. Chun, J.H. Lee, K.N. Kim, N.R. Kang, J.Y. Kim, M.H. Kim, K.S. Shin, M.K. Gupta, J.M. Baik, S.W. Kim, Adv. Mater. **26**, 5037 (2014)
31. H.Y. Mi, X. Jing, Q.F. Zheng, L.M. Fang, H.X. Huang, L.S. Turng, S.Q. Gong, Nano Energy **48**, 327–336 (2018)
32. Y. Feng, Y. Zheng, S. Ma, D. Wang, F. Zhou, W. Liu, Nano Energy **19**, 48 (2016)
33. H.Y. Li, L. Su, S.Y. Kuang, C.F. Pan, G. Zhu, Z.L. Wang, Adv. Funct. Mater. **25**, 5691 (2015)
34. S. Wang, Y. Zi, Y.S. Zhou, S. Li, F. Fan, L. Lin, Z.L. Wang, J. Mater. Chem. A **4**, 3728 (2016)
35. J. Luo, S. Gao, H. Luo, L. Wang, X. Huang, Z. Guo, X. Lai, L. Lin, R.K.Y. Li, J. Gao, Chem. Eng. J. **406**, 126898 (2021)